Structure and Oxygen Evolution Reaction Performance of Ni-supported Catalysts Based on Steam-Exploded Poplar

Junxia Yuan,[a] Xiaofei Li,[a] Feifan Wu,[a] Cheng Pan,[b,*] and Haitao Yang [a,*]

Using renewable steam-exploded poplar (SEP) as carbon source, nickel metal doped carbon hybrid materials were designed to synthesize catalysts (Ni/SEP) with certain oxygen evolution reaction (OER) properties and were compared with nickel catalysts supported on metal organic framework structure (ZIF67-Ni). The roles of SEP support in Ni-based catalyst were considered. Scanning electron microscope (SEM) images confirmed that the fiber could better hinder the aggregation of metal particles. Fourier transform infrared spectroscopy (FT-IR) indicated the presence of surface OH groups after the reduction process. X-ray diffraction (XRD) and X-ray photoelectron spectroscopy (XPS) analyses confirmed the major form of metallic Ni in the resulting Ni catalysts. Carbon materials as carriers, the synergetic effect of Ni-doped, and carbon carrier played an important role in facilitating the kinetics of OER, which was similar to the carrier of metal-organic frame material. Notably, the Ni/SEP (11.3 mF/cm^{-2}) and ZIF67-Ni (37.2 mF/cm^{-2}) with better OER performance exhibited a smaller double layer capacitances (Cdl), suggesting the intrinsic OER catalytic activity of the Ni/SEP and ZIF67-Ni were much higher in comparison to the ZIF67-Ni/SEP. Moreover, the inferior performance of Ni/SEP further indicated that the synergistic effect between carbon and Ni/NiO contributes to the enhanced OER activity.

DOI: 10.15376/biores.19.3.4886-4898

Keywords: Nickel supported catalyst; ZIF67; Steam explosion

Contact information: a: Hubei Provincial Key Laboratory of Green Materials for Light Industry, Hubei University of Technology, Wuhan, 430068, PR China; b: School of Chemical and Environmental Engineering, Wuhan Polytechnic University, Wuhan, 430023, China;
** Corresponding author: ch_pan1018@whpu.edu.cn; pphtyang1979@aliyun.com*

INTRODUCTION

The use of renewable biological resources to produce organic molecules has a long history and is increasingly employed in industrial chemistry. The products of agricultural, industrial or forestry waste materials are complex and difficult to separate, and how to convert the waste into specific products with specific properties and complexity is particularly critical. Other complex factors include the accumulation of excess chemicals in the product during use, natural aging, the recovery process itself and the interrelated flow of materials and products (Kümmerer *et al.* 2020). Demand for various metals, including copper, cobalt, nickel and lithium, required for the manufacture of renewable energy, electric vehicles, fuel cells, and storage technologies is expected to increase significantly in the coming decades. Many minerals and metals are considered to be "critical raw materials" or "technologically critical elements", and it is particularly important to design products with long life and reusability.

Nickel oxide (NiO) is a new type of mixed oxide catalyst with specific surface chemistry similar to that of effective oxide catalysts. The particles with smaller particle size have better catalytic activity (Pan *et al.* 2020). Nickel oxide has excellent redox properties, electrochemical properties, and gas sensing properties. Due to its high activity and low cost, it is widely used in catalytic oxidation. However, its industrial application is hindered by rapid coking and sintering. The results show that catalyst particle size, carrier defects, temperature-induced aggregation, and particle composition are the main factors leading to catalyst deactivation. It is necessary to prepare catalysts with adjustable metal dispersion density to improve the overall catalytic performance, but this remains a great challenge. The preparation methods of single-atom catalysts, such as single-atom catalyst synthesis strategy, atomic layer deposition techniques and host-guest cooperative protection strategies, all maximize the use of metal atoms to improve the active sites. However, single-atom electrocatalysts are still far from the real applications (Gong *et al.* 2019; Cao *et al.* 2020; Ji *et al.* 2020). To facilitate the recovery of catalysts, various materials have been used as carriers, including silica, alumina, titanium dioxide, zirconia, magnesia, and carbon. Metal-organic framework (MOF) is a kind of crystalline porous materials with a well-defined structure and diverse compositions, which not only shows great application potential in various fields, but also can be used as a carrier for the production of energy and catalytic materials. Stand-alone and binder-free MOF-based OER catalyst (Pan *et al.* 2020) showed excellent stability and efficient low overpotentials using an in-situ method. Some electrocatalysts with strong coupling to carbon were obtained by post-treatment of MOF. However, MOF is always composed of metal ions and expensive organic ligands, which is uneconomical and unsuitable for large-scale applications.

Due to the potentially high specific surface area of carbon, carbon materials can be used as carriers for metal particles. Nickel nanoparticles are coupled with carbon materials to solve the corrosion (oxidation) problem in harsh alkaline environment and increase the active area of nickel-based catalysts. Lignocellulosic materials are renewable and rich in hydroxyl groups, so they are promising carbon sources for the preparation of carbon carriers. In the process of preparation, it is meaningful to try to embed Ni nanoparticles directly into carbon materials to produce "embedded" catalysts (Du *et al.* 2020).

Steam explosion is an optional pretreatment technology in the field of biomass conversion. The particle size of different types of agricultural wastes treated by steam blasting is different. In the process of steam explosion treatment of biomass raw materials, high temperature and high-pressure conditions exacerbate the internal hydrogen bond breakage of cellulose, destroying the tight connection between cellulose, hemicellulose and lignin, increasing the specific surface area of cellulose, and improving the adsorption capacity of the steam explosion products. Preparation of catalysts using steam explosion products as carbon precursors is a feasible strategy to avoid aggregation, sintering, and loss of metal particles during pyrolysis.

Renewable, agricultural and forestry wastes, which are rich in hydroxyl groups, were used as the carbon source, and nickel metal doped carbon hybrid materials and their core-shell structures were designed to synthesize catalysts with certain OER properties for high value utilization. In this study, steam-exploded poplar was used as carbon source to support metal nickel to prepare catalyst. Results were compared with those obtained with nickel catalysts supported on metal organic framework structure (ZIF67-Ni). The catalysts were characterized using Fourier transform infrared spectroscopy (FT-IR), X-ray diffraction (XRD), N_2 adsorption-desorption, scanning electron microscope (SEM), and X-ray photoelectron spectroscopy (XPS). The OER performance and catalytic kinetics were

investigated using electrochemical tests (linear sweep voltammogram (LSV), Electrochemical Impedance Spectroscopy (EIS), cyclic voltammetry (CV), and electrochemical active surface area (ECSA)). The roles of steam-exploded poplar support in Ni-based catalyst were hereby discussed.

EXPERIMENTAL

Materials

Poplar was steam-exploded at 213 ℃ for 5 min. The compositional analysis of steam-exploded poplar (SEP) on a dry basis was carried out as described to determine the glucan (71.7%), xylan (4.0%), and lignin (13.0%) contents. All standards and chemical compounds, including xylose, glucose, arabinose, and cellulose, were chromatography grade and procured from Sigma-Aldrich (Shanghai, China). Nickel chloride hexahydrate, N,N-dimethylamide, 2-methylimidazole, ethanol, polyvinylpyrrolidone, methanol, ammonia, m-aminophenol, formaldehyde, and CTAB were analytical grade and procured from Sinopharm Chemical Reagent Co., Ltd. (Shanghai, China).

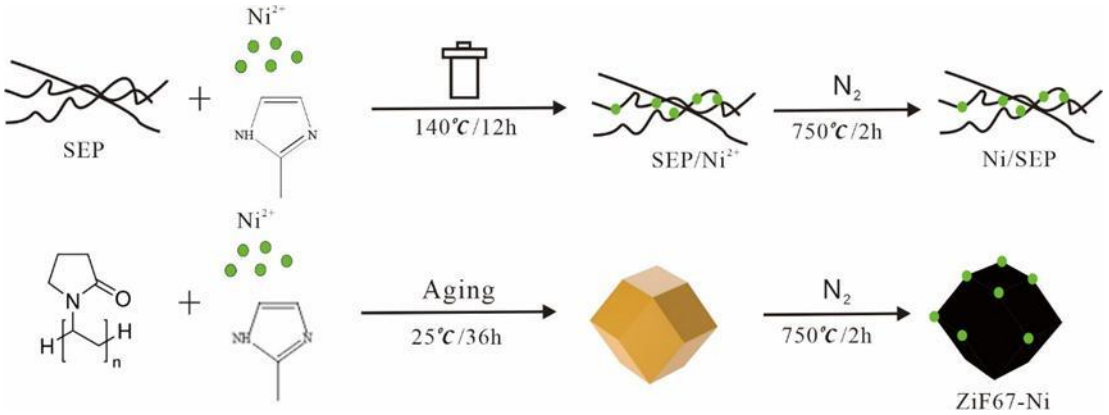

Fig. 1. Preparation of Ni/SEP, ZIF67-Ni and ZIF67-Ni/SEP

Methods

As shown in Fig. 1, 2 g SEP and 0.165 g nickel nitrate hexahydrate (0.02 mol) were ultrasonically dispersed in 10 mL of N, N-dimethylamide. In addition, 0.082 g (0.1 mol) of 2-methylimidazole was dissolved in 10 mL of N, N-dimethylamide. The two solutions were mixed and stirred evenly. Then they were added to a polytetrafluoroethylene reactor and reacted at 140 ℃ for 12 h. After natural cooling, the product was centrifuged with anhydrous ethanol and distilled water and dried in vacuum. The obtained product was used to pyrolyze the feedstock as follows: the temperature was increased at a rate of 5 ℃/min under nitrogen protection, and the feedstock was held for 2 h at 750 ℃ and subsequently cooled to room temperature inside the furnace. The carbon material was hereafter referred to as Ni/SEP.

Next, 0.75 g polyvinylpyrrolidone and 1.19 g nickel nitrate hexahydrate (0.005 mol) were ultrasonic dispersed in 50 mL of methanol. In addition, 3.3 g (0.04 mol) 2-methylimidazole was dissolved in 50 mL of methanol. The two solutions were mixed and stirred evenly, then placed at room temperature for 36 h, centrifuged, and dried in vacuum. The obtained product was used to pyrolyze the feedstock under the same conditions of

Ni/SEP, to obtain ZIF67-Ni. During the preparation under the same conditions as ZIF67-Ni, 0.15 g of SEP was added to obtain the final product named ZIF67-Ni/SEP.

Characterization

The crystal structure of the sample was analyzed by Ultima IV X-ray diffractometer. The working voltage of the X-ray diffractometer was 40 kV, and the current density was 30 mA. X-ray photoelectron spectroscopy (XPS) analysis was carried out by using an ESCALAB 250 analyzer (Thermo Science) and a monochromatic Al Ka X-ray source. The Fourier transform infrared spectrometer (Karlsruebrook, Germany) used KBr pellet technology to measure FT-IR in the wavelength range of from 4000 to 400 cm^{-1}. The ZEISS Merlin roller was observed by scanning electron microscope (SEM) under 10kV voltage. The adsorption-desorption isotherm of nitrogen was determined by BELSORP-mini II instrument and Brunauer-Emmett-Teller (BET) method (Alam *et al.* 2018).

Electrochemical Characterization

Electrochemical measurements were performed at room temperature using a three-electrode setup with the CHI760E electrochemical workstation. The glassy carbon electrode was the working electrode (counter electrode) and the Ag/AgCl electrode was the reference electrode. Linear sweep voltammogram (LSV) was recorded at a scanning rate of 5 mV/s in 1.0 M KOH electrolyte. The scanning range was 1. 0-1.8vs.RHE. The linear sweep voltammetry curves were obtained at a scan rate of 5mV/s, and corrected by the 90% IR compensation method. The measured potentials E_{Appl} (vs.Ag/AgCl) were converted to the corresponding reversible hydrogen electrode potentials (E_{RHE}) according to the Nernst equation ($E_{RHE}=E_{Ag/AgCl}+0.059\cdot pH+0.197$). The current density ($J$) was taken as its absolute value and the overpotential (η) of the OER at a current density of 10 mA/cm^2 was calculated using the equation ($\eta = E_{RHE}-1.23V$). According to the Tafel equation ($\eta = a+b\cdot\log(J)$), the Tafel slope (b) could be obtained by fitting the linear part of the Tafel curve. The voltage measured by electrochemical impedance spectroscopy was at 1.524 V (*vs.* RHE) with a frequency range of 100 kHz and an AC voltage of 5 mV. The electrochemical active surface area (ECSA) was estimated by measuring the electrochemical double layer capacitance (Cdl) of the catalyst. The Cdl was measured by using the cyclic voltammetry curve of the illegal Laday zone at 1.12V (*vs*. RHE) at different scan rates (*vs.* 10, 20, 30, 40, and 50 mV/s). The calculation formula of electrochemical active surface area (ECSA) was: ECSA=Cdl/Cs (Cs is about 0.040 mF) (Cao *et al.* 2018; Lan *et al.* 2018; Pan *et al.* 2022).

RESULTS AND DISCUSSION

SEM micrographs reveal the morphology of the Ni/SEP, ZIF67-Ni/SEP, and ZIF67-Ni, as shown in Fig. 2. The irregular carbonized fibers and interconnected structure originates from the natural structure of the SEP are shown in Figs. 2a and 2b. The surface morphology and naturally wrinkled surface of the carbonized fibers indicated that the biological fiber network structure and inner porous structure of the SEP were well retained after carbonization. Ni nanoparticles were uniformly distributed and partially covered by graphite sheets. The EDX spectrum of the Ni/SEP composite proved the existence of Ni (Fig. 2d). The nickel particles (Fig. 2a, b) attached to the fiber surface had a particle size

of less than 100 nm, whereas the spherical diameter of ZIF67-Ni (Fig. 2c) was approximately 400 nm. High-resolution scanning electron microscopic (SEM) image confirmed that the fibers can better hinder the aggregation of metal particle.

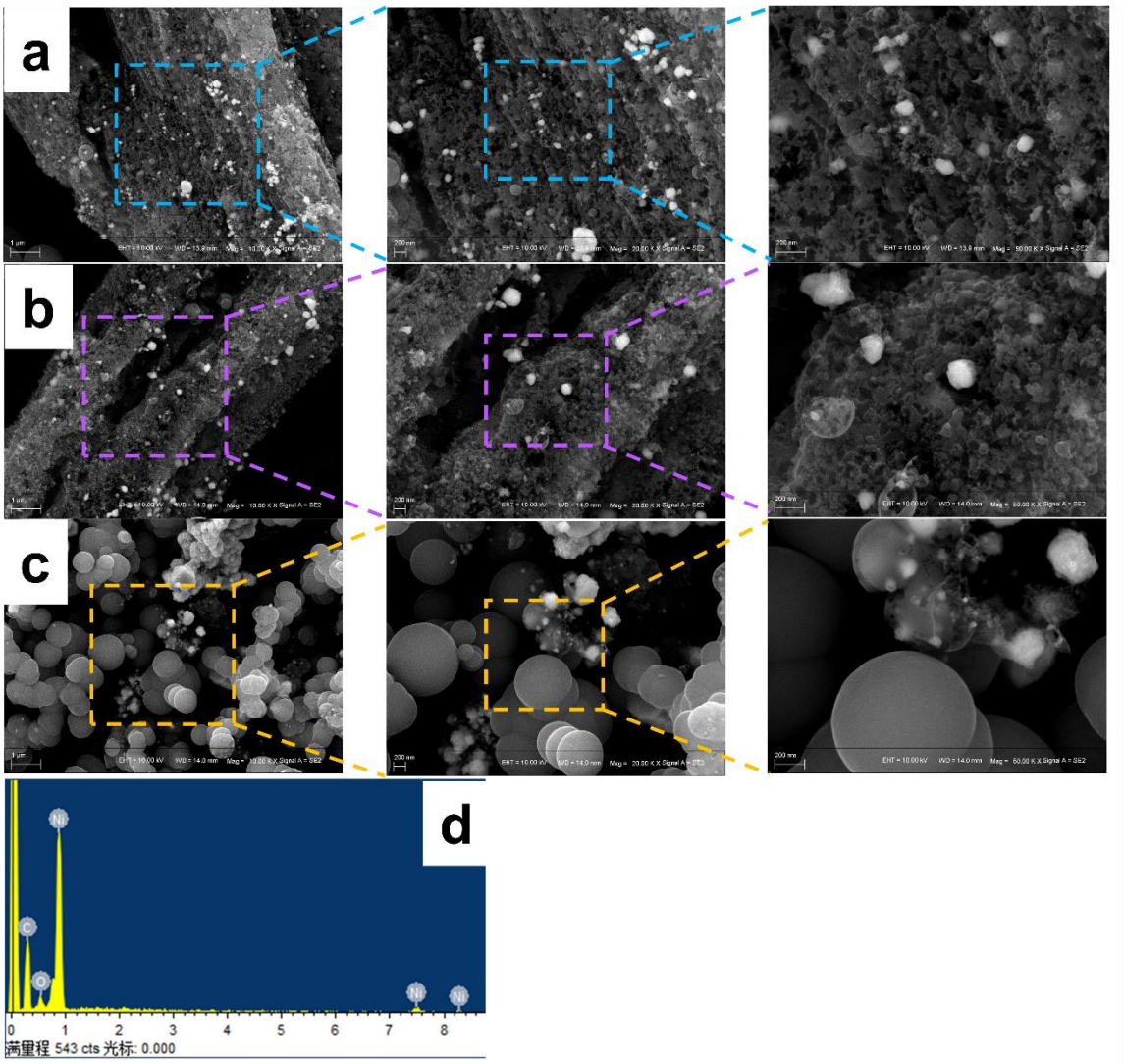

Fig. 2. SEM images of Ni/SEP (a), ZIF67-Ni/SEP (b), ZIF67-Ni (c) and EDX (d)

The FT-IR spectra of Ni/SEP, ZIF67-Ni/SEP, and the ZIF67-Ni nanocomposite are shown in Fig. 3a. The FT-IR spectra showed strong absorption of infrared light at 3442 and 1639 cm^{-1}, which can be attributed to the stretching modes of absorbed water (Yan *et al.* 2018; Gaidukevič *et al.* 2018; Dong *et al.* 2018). The FT-IR spectra showed the peak at 2922 cm^{-1} originated from C-H, and the bands at 1738 cm^{-1} correspond to the C=O of the oxygen-containing functional groups. The shoulder peak near 1404 cm^{-1} corresponds to the bending vibration of OH group δ(OH), as has been predicted by infrared spectroscopy studies (Zhang *et al.* 2015; Negar *et al.* 2018), which indicated presence surface OH groups after reduction process. The peaks that emerge at 673 cm^{-1} for Ni/SEP, ZIF67-Ni/SEP and ZIF67-Ni could be ascribed to symmetric Ni-O stretching.

As shown in Fig. 3b, the X-ray diffraction (XRD) patterns of Ni/SEP, ZIF67-Ni/SEP, and ZIF67-Ni all show three sharp diffraction peaks at approximately 44.49°,

51.83°, and 76.29°, corresponding to the (111), (200), and (220) crystal planes of NiO (Ref. Code 01-070-1849), respectively, indicating the predominant formation of metallic Ni in the samples. The diffraction pattern of ZIF67-Ni/SEP and ZIF67-Ni had three peaks at 37.23°, 43.31°, and 62.88°, corresponding to (111), (200), and (220) of NiO (Ref. Code 00-001-1239), respectively (Wang *et al.* 2008; Zhu *et al.* 2009). The absence of corresponding peaks in Ni/SEP was related to the structure of organic ligands. The average crystallite size was determined to be about 35.37 nm for Ni/SEP, 47.93 nm for ZIF67-Ni/SEP, and 35.93 nm for ZIF67-Ni from the (111) reflection by utilizing Scherrer's equation relating the coherently scattering domains with Bragg peak widths: $D = k\lambda/B\cos(\theta)$, in which $k = 0.89$ for spherical particles and B is the full angular width at half-maximum of the peak in radians. These results showed that the nickel metal particles were well dispersed on the surface of the fiber.

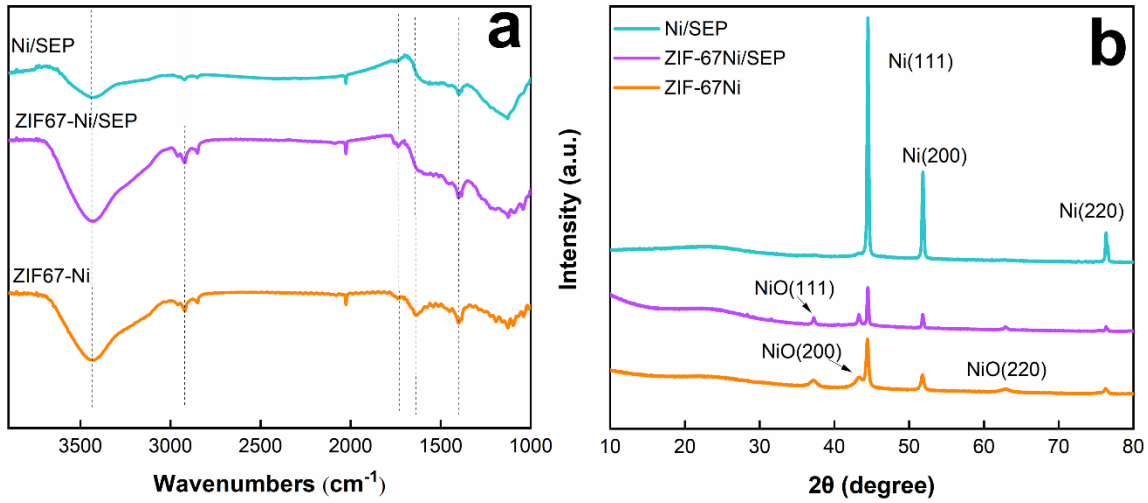

Fig. 3. FT-IR (a) and XRD (b) spectra of Ni/SEP, ZIF67-Ni/SEP and ZIF67-Ni

The XPS results confirmed that all C1s (Fig. 4I), N1s (Fig. 4II), Ni2p (Fig. 4III), and O1s (Fig. 4IV) were in the samples. The atomic percents of Ni2p were 0.76%, 0.53%, and 2.11% for Ni/SEP (a), ZIF67-Ni/SEP (b), and ZIF67-Ni (c), respectively. As shown in Supplementary Fig. In Fig. 4II, N-C bonds in the samples of Ni/SEP, ZIF67-Ni/SEP and ZIF67-Ni were in the form of N-Ni (398.58 eV), pyrrolic N (400.98 eV), and pyridinic N (402.98 eV). The quantitative analysis of XPS results showed that the atomic ratios of N/C in Ni/SEP, ZIF67-Ni/SEP, and ZIF67-Ni were 8.72:84.07, 8.99:83.46 and 7.53:84.16, respectively. The presence of N dopant in the samples inherently improved the interaction ability with the reactants and produce higher positive charge density on its adjacent carbon atoms, which may also contribute to the high activity of the sample (Zou *et al.* 2014).

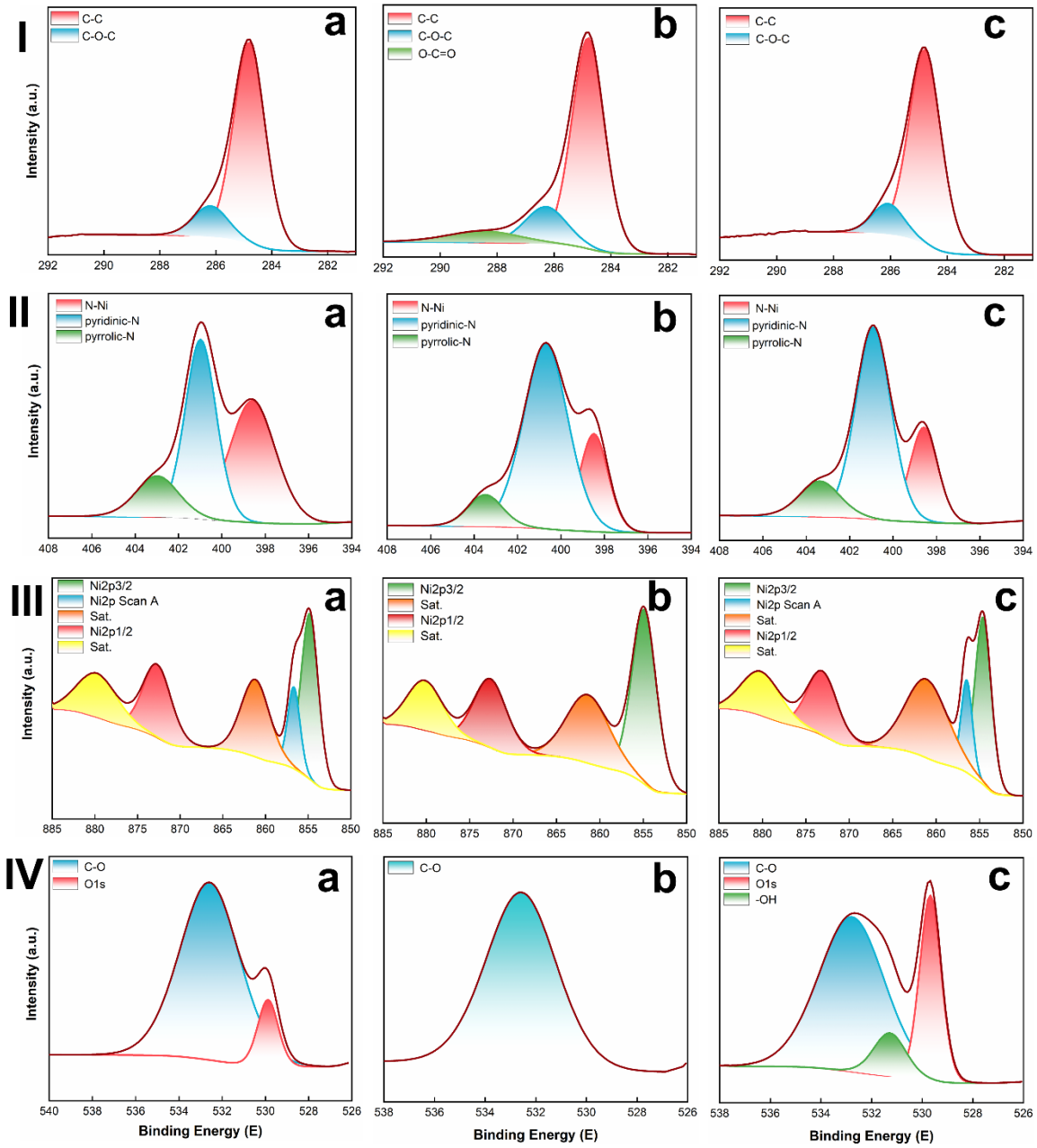

Fig. 4. High-resolution XPS spectra of C1s (Ⅰ), N1s (Ⅱ), Ni2p (Ⅲ), O1s (Ⅳ) of Ni/SEP (a), ZIF67-Ni/SEP (b) and ZIF67-Ni (c)

As shown in Fig. 4I, the three components of the C1s spectrum (284.78, 286.08 and 288.58 eV) were attributed to C-C, C-O-C, and O-C-O, respectively. The amount of C-O in ZIF67-Ni (10.93%) was higher than that in Ni/SEP (6.54%) and ZIF67-Ni/SEP, which confirmed the slight oxidation of carbon. The XPS spectrum (Fig. 4IV) for O 1s of samples can be deconvoluted into two peaks at binding energies of 529.78 and 532.68 eV, which were attributed to surface adsorbed water (-OH) and C-O species, respectively. Compared with that in Ni/SEP (9.90%) and ZIF67-Ni/SEP (15.35%), emerging peak in ZIF67-Ni (20.06%) attributed to metal oxide species (Ni-O bond) at 528.88 eV confirmed the formation of Ni-O. These findings can be confirmed by Ni2p spectra corresponding to the strong peak at 861.18 eV of Ni-O. In addition, the curve fitting results of the Ni2p spectrum

in Fig. 4III shown the fitting ratio of Ni0 (854.58 and 873.18 eV) and Ni^{2+} (861.18 and 880.38 eV) were 35.63% and 33.16%, respectively, which can be attributed to Ni-Ni and Ni-O bonding. Based on XPS analysis, the ZIF67-Ni had a slightly higher loading of Ni^{2+} than the sample containing carbon carrier. Both XRD and XPS analyses confirmed the major form of metallic Ni rather than single Ni atoms in the resulting Ni catalysts.

The specific surface area and porosity of the samples were investigated by N_2 adsorption-desorption experiments. In the curves of Ni/SEP, ZIF67-Ni/SEP, and ZIF67-Ni (Fig. 5a), the type IV adsorption branches were corresponding to the mesoporous structure. As shown in Fig. 5b, the specific surface areas of Ni/SEP and ZIF67-Ni were calculated to be 323 and 429 $m^2 \cdot g^{-1}$, respectively. Compared with Ni/SEP and ZIF67-Ni, ZIF67-Ni/SEP had relatively higher specific surface area, which might be due to the fact that SEP as a carrier could reduce the aggregation and agglomeration of ZIF67-Ni particles. The pore size distributions were shown in Fig. 5c.

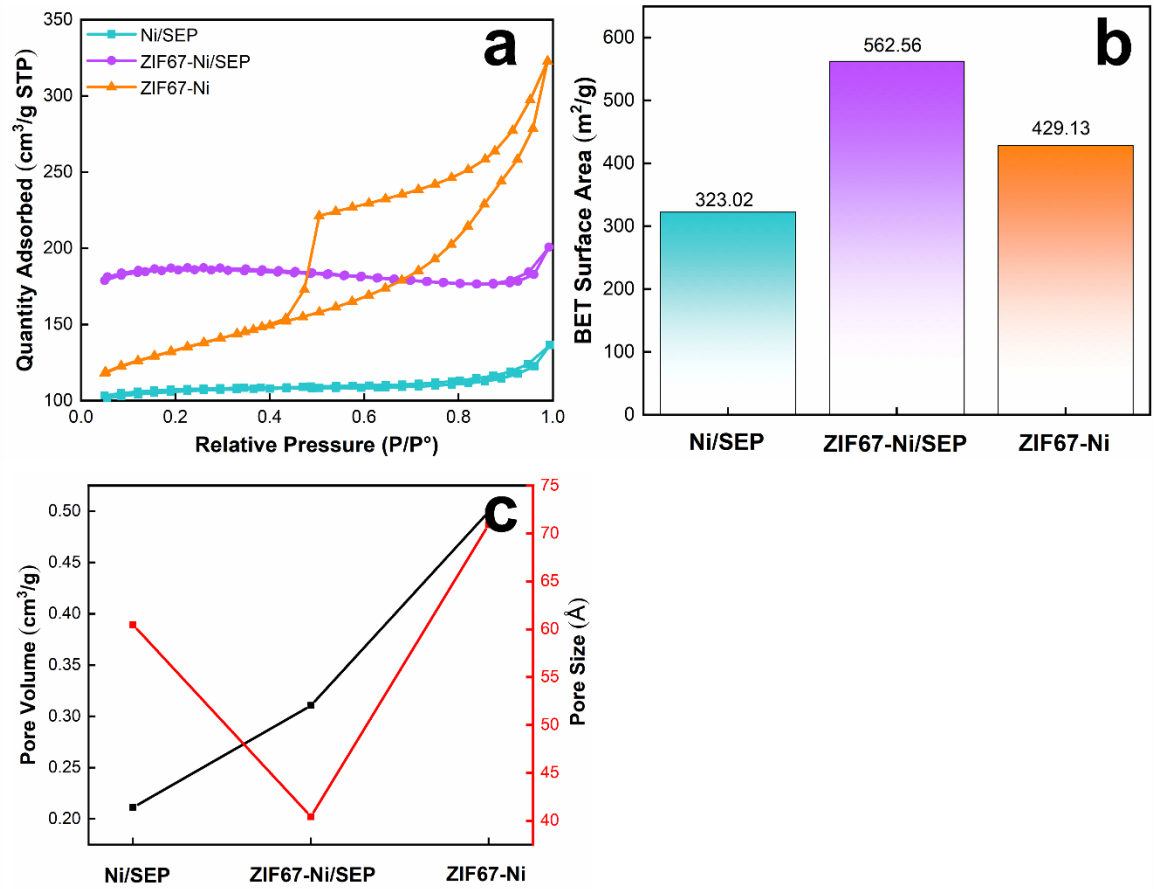

Fig. 5. N_2 adsorption-desorption curves (a), specific surface area (b), pore volume and pore diameter (c) of Ni/SEP, ZIF67-Ni/SEP and ZIF67-Ni

The average pore size of ZIF67-Ni/SEP was 35.05 nm, while those of Ni/SEP and ZIF67-Ni were 6.67 nm and 5.62 nm, respectively. It was clear that Ni/SEP and ZIF67-Ni/SEP were mainly composed of micropores and mesopores between 1 and 5 nm. Compared with ZIF67-Ni, the micropore proportion of Ni/SEP and ZIF-67Ni/SEP were higher, which indicated that the doping of nickel particles can effectively regulate the micropore structure through the chemical reaction with carbon (Ubago-Perez *et al.* 2016).

As shown in Fig. 5c, the average pore widths of three samples were in the order of ZIF67-Ni/SEP > ZIF67-Ni > Ni/SEP, and the pore volumes of Ni/SEP, ZIF67-Ni/SEP, and ZIF67-Ni were 0.21, 0.31, and 0.50 $cm^3 \cdot g^{-1}$, respectively. The pore structure of materials played an important and even decisive role in many properties of materials. The carbon materials served as carriers. The porous properties facilitated the diffusion of small molecules onto the substrates and can expose more active sites, thus improving the overall activity of the catalyst.

The electrocatalytic OER performance of Ni/SEP, ZIF67-Ni/SEP, and ZIF67-Ni were studied in O^{2-} saturated in 1.0 M KOH electrolyte at a scan rate of 5 mV / s. The scan range was 1.0 to 1.8 *vs.* RHE. The linear sweep voltammograms (LSVs) data (Fig. 6a and b) was recorded with the scan rate of 5 $mV \cdot s^{-1}$. Both Ni/SEP and ZIF67-Ni showed that the Ni^{2+}/Ni^{3+} was oxidized in the potential range of 1.33 to 1.42 V (all potentials were versus reversible hydrogen electrode (RHE)). The existence of the oxidation peak indicated that insufficient oxidation may not form a fully protected NiO shell outside the Ni nanoparticles, leading to corrosion of metal Ni and the formation of NiOOH during OER in alkaline solution (Li *et al.* 2020). Polarization curves (Fig. 7a and b) showed that ZIF67-Ni exhibited excellent OER performance with an overpotential of 420 mV at 10 $mA \cdot cm^{-2}$ current density, compared to Ni/SEP (504 mV) and ZIF67-Ni/SEP (0), respectively.

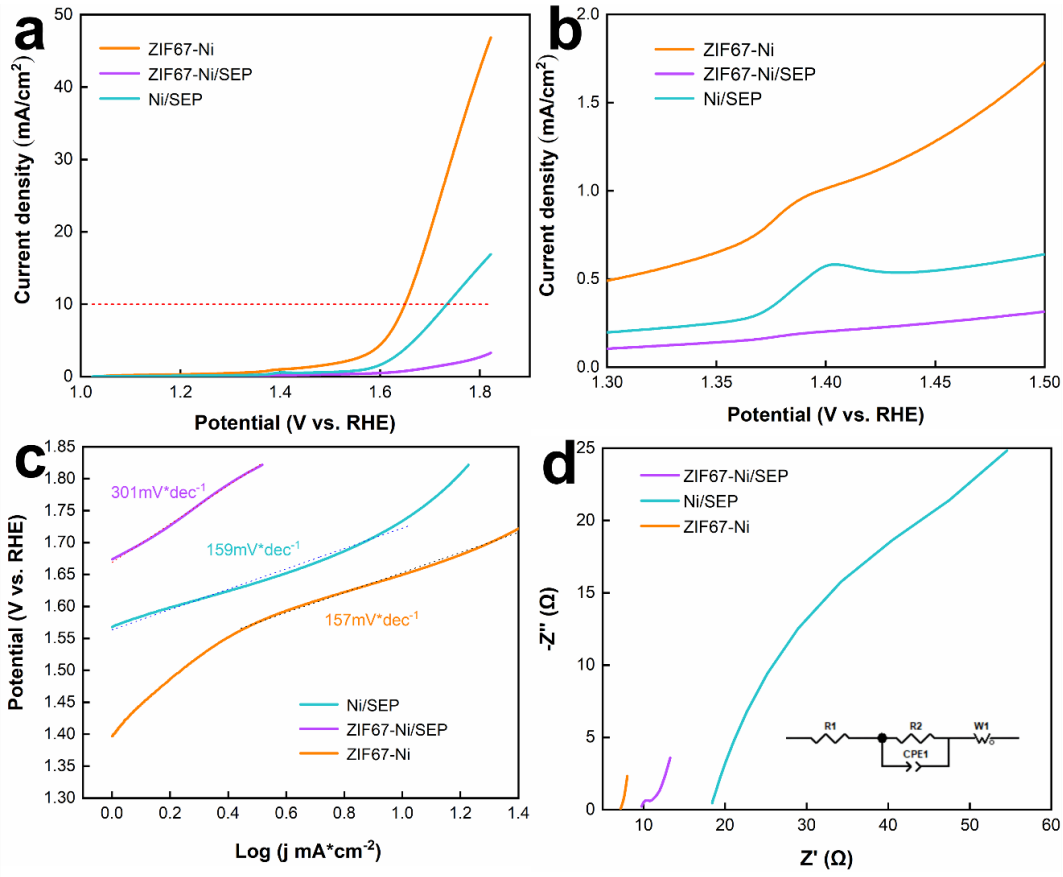

Fig. 6. (a) LSV curves of Ni/SEP, ZIF67-Ni/SEP and ZIF67-Ni; (b) The amplification of (a) from 1.30 to 1.50 V (*vs*. RHE); (c) Tafel slopes of all the samples; (d) EIS plots.

To investigate the kinetics of these catalysts, the Tafel slopes obtained from the LSV polarization curves are shown in Fig. 6c. The Tafel slope of ZIF67-Ni (157 $mV \cdot dec^{-1}$)

was close to that of Ni/SEP (159 mV·dec^{-1}), and considerably smaller than those of ZIF67-Ni/SEP (301 mV·dec^{-1}), confirming its fastest OER kinetics. Based on the above results, the synergetic effect of Ni-doped and carbon carrier played an important role in facilitating the kinetics of OER (Jian *et al.* 2018; Yue *et al.* 2019), which was similar to that of materials with metal-organic framework structures as carriers. The Nyquist plots (Fig. 6d) were fitted to a simplified Randles equivalent circuit model. The very small semicircles in the high frequency zone were attributed to the internal charge-transfer resistances (Rct(int)) of the electrodes (Burke *et al.* 2015). Among all the samples, ZIF67-Ni showed the lowest charge transfer resistance (Rct=7.1), indicating the highest charge transfer efficiency during OER (Li *et al.* 2020), which was confirmed by the Tafel slope results.

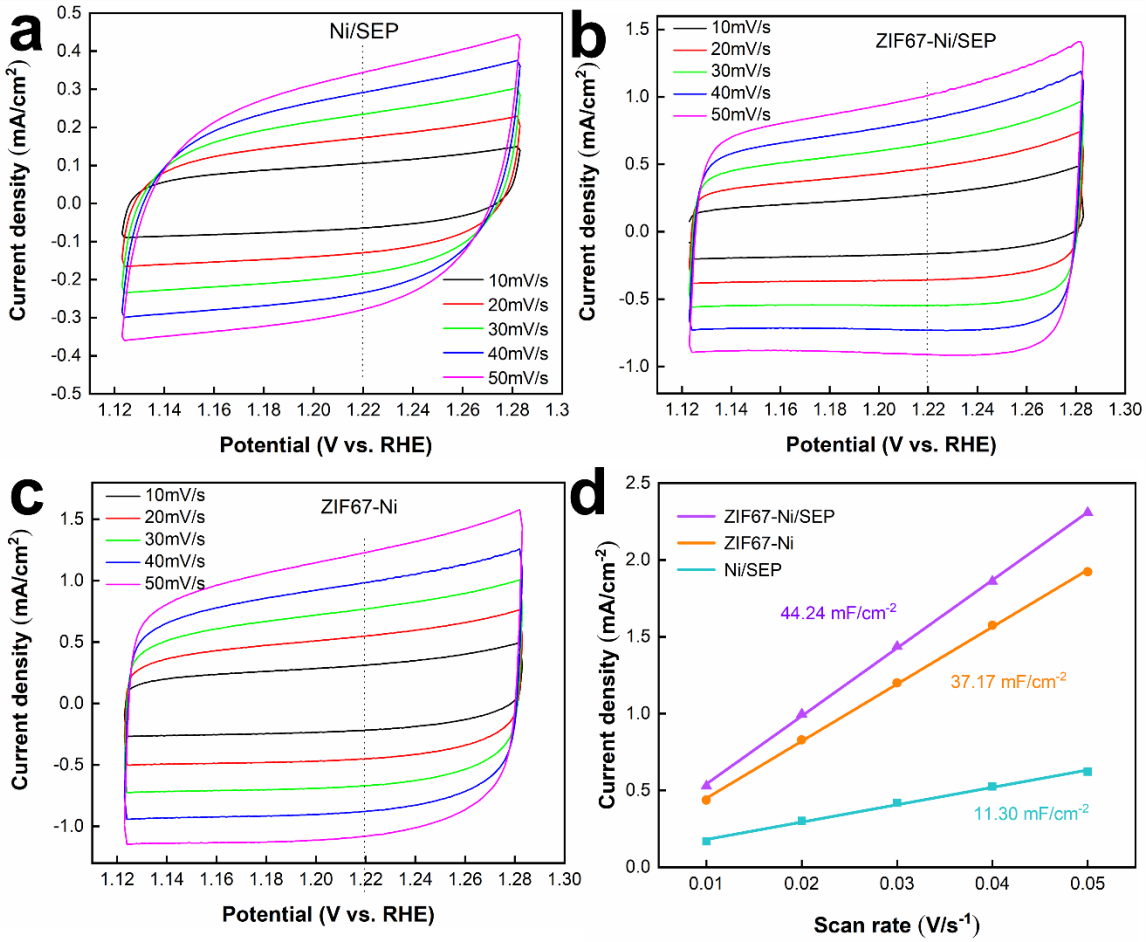

Fig. 7. (a-c) CV curves of Ni/SEP, ZIF67-Ni/SEP and ZIF67-Ni at different scanning rates in non-faradic region; (d) Cdl values of all samples

Cyclic voltammetry (CV) curves were measured in a region from 1.12 to 1.22 V *vs.* RHE (scanning rates ranged from 10 to 50 mV·s^{-1}) to calculate the double layer capacitances (Cdl) (Fig. 7), as an important parameter for estimating the ECSA (Ma *et al.* 2014). As shown in Fig. 7d, compared with Ni/SEP (11.30 mF·cm^{-2}) and ZIF67-Ni (37.17 mF·cm^{-2}), the synthesized ZIF67-Ni/SEP possessed a higher Cdl value (44.24 mF·cm^{-2}), which was supposed to originate from the SEP carrier of the catalyst, providing a large and effective electrocatalyst-electrolyte contact interface area. The results were positively related with BET specific surface area. Notably, the Ni/SEP and ZIF67-Ni with better OER

performance showed smaller Cdl than ZIF67-Ni/SEP, suggesting the intrinsic OER catalytic activity of the Ni/SEP and ZIF67-Ni were much higher in comparison to the ZIF67-Ni/SEP (Pan *et al.* 2020). Moreover, the inferior performance of Ni/SEP further indicated that the synergistic effect between carbon and Ni/NiO contributes to the enhanced OER activity (Yue *et al*. 2019). These results demonstrated that Ni/SEP has similar activity for OER compared with ZIF67-Ni.

CONCLUSIONS

1. Using renewable steam-exploded poplar wood as carbon sources, nickel metal doped carbon hybrid materials were designed to synthesize catalysts with certain oxygen evolution reaction (OER) properties.
2. Compared with the known catalyst ZIF67-Ni, nickel supported on steam-exploded poplar (Ni/SEP) had similar activity for OER.
3. The porous nature of the carbon material facilitated the diffusion of substrates, which can expose more active sites and improve the overall activity of the catalysts; the fiber can better hinder the aggregation of metal particles, and the OH group on the surface still existed after reduction process; smaller Cdl suggested the intrinsic OER catalytic activity of the Ni/SEP and ZIF67-Ni; the inferior performance of Ni/SEP further indicated that the synergistic effect between carbon and Ni/NiO contributes to the enhanced OER activity.

ACKNOWLEDGMENTS

The authors are grateful for the support of the National Nature Science Foundation of China (NSFC, No. 21978074).

REFERENCES CITED

Alam, N., Oskam, E., Stassen, P. M., Exter, P. V., Ven, P. M., Haak, H. R., Hoolleman, F., Zanten, A. V., Nguyen, H. V., Bon, V., Duineveld, B. A. M., *et al.* (2018). "Prehospital antibiotics in the ambulance for sepsis: A multicentre, open label, randomised trial," *National Library of Medicine* 6, 40-50. DOI: 10.1016/S2213-2600(17)30469-1

Burke, M. S., Kast, M. G., Trotochaud, L., Smith, A. M., and Boettcher, S. W. (2015). "Cobalt-iron (oxy)hydroxide oxygen evolution electrocatalysts: The role of structure and composition on activity, stability, and mechanism," *Journal of the American Chemical Society* 137(10), 3638-3648. DOI: 10.1021/jacs.5b00281

Cao, L. N., Liu, W., Luo, Q. Q., Yin, R. T., Wang, B., Weissenrieder, J., Soldemo, M., Yan, H., Lin, Y., Sun, Z. H., *et al*. (2019). "Atomically dispersed iron hydroxide anchored on Pt for preferential oxidation of CO in H_2," *Nature* 565, pages 631-635. DOI: 10.1038/s41586-018-0869-5

Cao, Y. Q., Zhang, H., Ji, S. F., Sui, Z. J., Jiang, Z., Wang, D. S., Zaera, F., Zhou, X. G., Duan, X. Z., and Li, Y. D. (2020). "Adsorption site regulation to guide atomic design

of Ni–Ga catalysts for acetylene semi-hydrogenation," *Angewandte Chemie International Edition* 59, 11647-11652. DOI: 10.1002/anie.202004966

Dong, Y. T., Ma, Y. H., Li, D., Liu, Y. H., Chen, W. H., Feng, X. M., Zhang, J. M. (2018). "Construction of 3D architectures with $Ni(HCO_3)_2$ nanocubes wrapped by reduced graphene oxide for LIBs: Ultrahigh capacity, ultrafast rate capability and ultralong cycle stability," *Chemical Science* 9, 8682-8691. DOI: 10.1039/C8SC02868K

Du, B. Y., Liu, C., Wang, X., Han, Y., Guo, Y. Z., Li, H. M., and Zhou, J.H. (2020). "Renewable lignin-based carbon nanofiber as Ni catalyst support for depolymerization of lignin to phenols in supercritical ethanol/water," *Renewable Energy* 147, 1331-1339. DOI: 10.1016/j.renene.2019.09.108

Gaidukevič, J., Pauliukaitė, R., Niaura, G., Matulaitienė, I., Opuchovič, O., Radzevič, A., Astromskas, G., Bukauskas, V., and Barkauskas, J. (2018). "Synthesis of reduced graphene oxide with adjustable microstructure using regioselective reduction in the melt of boric acid: Relationship between structural properties and electrochemical performance," *Nanomaterials* 8(11). DOI: 10.3390/nano8110889

Gong, Y.N., Jiao, L., Qian, Y.Y., *et al.* (2019). "Regulating the coordination environment of MOF-templated single-atom nickel electrocatalysts for boosting CO_2 reduction," *Angewandte Chemie-international Edition* 59, 2705-2709. DOI: 10.1002/anie.201914977

Jiang, J., Sun, F. F., Zhou, S., Wei, H., Zang, H., Dong, J. C., Jiang, Z., Zhao, J. J., Li, j. f., Yan, W. S., *et al.* (2018). "Atomic-level insight into super-efficient electrocatalytic oxygen evolution on iron and vanadium co-doped nickel(oxy) hydroxide," *Nature Communications* 9, article 2885. DOI: 10.1038/s41467-018-05341-y

Ji, S. F., Qu, Y., Wang, T., Chen, Y. J., Wang, G. F., Li, X., Dong, J. C., Chen, Q. Y., Zhang, W. Y., Zhang, Z. D., *et al*. (2020). "Rare-earth single erbium atoms for enhanced photocatalytic CO_2 reduction," *Angewandte Chemie-international Edition* 59, 10651-10657. DOI: 10.1002/anie.202003623

Kümmerer, K., Clark, J. H., and Zuin, V. G. (2020). "Rethinking chemistry for a circular economy," *Science* 367, 369-370. DOI: 10.1126/science.aba4979

Lan, K., Li, J., Zhu, Y., Gong, L., Li, F., Jiang, P. B., Niu, F., and Li, R. (2018). "Morphology engineering of $CoSe_2$ as efficient electrocatalyst for water splitting," *Journal of Colloid and Interface Science* 539, 646-653. DOI: 10.1016/j.jcis.2018.12.044

Li, Y. Y., Huang, J. W., Rao, G. F., Wu, C. Y., Du, X. C., Sun, Y. H., Wang, X. F., and Yang, C. T. (2020). "Enhanced water oxidation activity of 3D porous carbon by incorporation of heterogeneous Ni/NiO nanoparticles," *Applied Surface Science* 530, article 147192. DOI: 10.1016/j.apsusc.2020.147192

Ma, T. Y., Dai, S., Jaroniec, M., and Qiao, S. Z. (2014). "Metal-organic framework derived hybrid Co_3O_4-carbon porous nanowire arrays as reversible oxygen evolution electrodes," *Journal of the American Chemical Society* 136(39), 13925-13931. DOI: 10.1021/ja5082553.

Negar, A., Abdollah, S., Rahman, H., Fardin, F., and Farzad, S. (2018). "Ni-hemin metal-organic framework with highly efficient peroxidase catalytic activity: Toward colorimetric cancer cell detection and targeted therapeutics," *Journal of Nanobiotechnology* 16(1), 93. DOI: 10.1186/s12951-018-0421-7

Pan, C. C., Liu, Z. C., and Huang, M. H. (2020). "2D iron-doped nickel MOF nanosheets grown on nickel foam for highly efficient oxygen evolution reaction," *Applied*

Surface Science 529, article 147201. DOI: 10.1016/j.apsusc.2020.147201

Pan, C., Yang, G. Y., Yang, H. T., Wang, L., Jiang, J. G., Zhang, Y. F., and Wu, F. F. (2022). "Facile fabrication of steam-exploded poplar loaded with non-metal-doped Ni-Fe nanoparticles: Catalytic activities in 4-nitrophenol reduction and electrocatalytic reaction," *Arabian Journal of Chemistry* 15, article 103944. DOI: 10.1016/j.arabjc.2022.103944.

Ubago-Perez, R., Carrasco-Marin, F., Fairen-Jimenez, D., and Moreno-Castilla, C. (2006). "Granular and monolithic activated carbons from KOH-activation of olive stones," *Microporous and Mesoporous Materials* 92, 64-70. DOI: 10.1016/j.micromeso.2006.01.002

Wang, H. Z., Kou, X. L., Zhang, J., and Li, J. G. (2008). "Large scale synthesis and characterization of Ni nanoparticles by solution reduction method," *Bulletin of Materials Science* 31(1), 97-100. DOI: 10.1007/s11671-009-9279-9

Yan, Z. H., Sun, H. M., Chen, X., Liu, H. H., Zhao, Y. R., Li, H. X., Xie, W., Cheng, F. Y., and Chen, J. (2018). "Anion insertion enhanced electrodeposition of robust metal hydroxide/oxide electrodes for oxygen evolution," *Nature Communications* 9(1), article 2373. DOI: 10.1038/s41467-018-04788-3

Yue, S., Wang, S. S., Jiao, Q. Z., Feng, X. T., Zhan, K., Dai, Y. Q., Feng, C. H., Li, H. S., Feng, T. Y., and Zhao, Y. (2019). "Preparation of yolk-shell-structured CoxFe1-xP with enhanced OER performance," *ChemSusChem* 12(19), 4461-4470. DOI: 10.1002/cssc.201901604

Zhang, C., Dabbs, D. M., Liu, L. M., Aksay, I. A., Car, R., and Selloni, A. (2015). "Combined effects of functional groups, lattice defects, and edges in the infrared spectra of graphene oxide," *The Journal of Physical Chemistry C* 119(32), 18167-18176. DOI: 10.1021/acs.jpcc.5b02727

Zhu, L.P., Liao, G. H., Yang, Y., Xiao, H. M., Wang, J. F., and Fu, S. Y. (2009). "Self-assembled 3D flower-like hierarchical β-$Ni(OH)_2$ hollow architectures and their *in situ* thermal conversion to NiO," *Nanoscale Research Letters* 4, article 550. DOI: 10.1007/s11671-009-9279-9

Zou, X. X., Huang, X. X., Goswami, A., Silva, R., and Asefa, T. (2014). "Cobalt-embedded nitrogen-rich carbon nanotubes efficiently catalyze hydrogen evolution reaction at all pH values," *Angewandte Chemie* 53(17), 4372-4376. DOI: 10.1002/ange.201311111

Article submitted: September 21, 2023; Peer review completed: December 16, 2024; Revised version received and accepted: February 29, 2024; Published: June 4, 2024.
DOI: 10.15376/biores.19.3.4886-4898